Journal of Instrumentation

SISSA

OPEN ACCESS

Characterisation of the Hamamatsu photomultipliers for the KM3NeT Neutrino Telescope

To cite this article: S. Aiello *et al* 2018 *JINST* **13** P05035

View the article online for updates and enhancements.

Related content

- Qualification tests of the R11410-21 photomultiplier tubes for the XENON1T detector
P. Barrow, L. Baudis, D. Cichon et al.
- The optical modules of the phase-2 of the NEMO project
S Aiello, E Leonora, F Ameli et al.
- Expansion cone for the 3-inch PMTs of the KM3NeT optical modules
The KM3NeT collaboration

Recent citations

- Characterisation of the Hamamatsu R12199-01 HA MOD photomultiplier tube for low temperature applications
M.A. Unland Elorrieta *et al*
- STRAW (STRings for Absorption length in Water): pathfinder for a neutrino telescope in the deep Pacific Ocean
M. Boehmer *et al*

IOP ebooks™

Bringing together innovative digital publishing with leading authors from the global scientific community.

Start exploring the collection–download the first chapter of every title for free.

This content was downloaded from IP address 151.97.200.161 on 26/06/2020 at 08:20

Jinst

Published by IOP Publishing for Sissa Medialab

Received: *December 29, 2017*
Accepted: *April 23, 2018*
Published: *May 31, 2018*

Characterisation of the Hamamatsu photomultipliers for the KM3NeT Neutrino Telescope

The KM3NeT collaboration

S. Aiello,[p] S.E. Akrame,[c] F. Ameli,[t] E. G. Anassontzis,[y] M. Andre,[ar] G. Androulakis,[aa] M. Anghinolfi,[q] G. Anton,[f] M. Ardid,[as] J. Aublin,[au] T. Avgitas,[au] M. Baars,[ab] C. Bagatelas,[aa] G. Barbarino,[r,am] B. Baret,[au] J. Barrios-Martí,[j] A. Belias,[aa] E. Berbee,[ab] A. van den Berg,[i] V. Bertin,[b] S. Biagi,[l] A. Biagioni,[t] C. Biernoth,[f] R. Bormuth,[ab,v] J. Boumaaza,[w] S. Bourret,[au] M. Bouwhuis,[ab] C. Bozza,[ap] H.Brânzaş,[u] N. Briukhanova,[q,x] R. Bruijn,[aw] J. Brunner,[b] E. Buis,[af] R. Buompane,[r,ai] J. Busto,[b] D. Calvo,[j] A. Capone,[aq,t] L. Caramete,[u] S. Celli,[aq,t,h] M. Chabab,[c] S. Cherubini,[l,ak] V. Chiarella,[m] T. Chiarusi,[o] M. Circella,[n] R. Cocimano,[l] J.A.B. Coelho,[au] A. Coleiro,[j] M. Colomer Molla,[au,j] R. Coniglione,[l] P. Coyle,[b] A. Creusot,[au] G. Cuttone,[l] A. D'Onofrio,[r,ai] R. Dallier,[ad] C. De Sio,[ap] I. Di Palma,[aq,t] A.F. Díaz,[ah] C. Distefano,[l] A. Domi,[q,b,al] R. Donà,[o,aj] C. Donzaud,[au] D. Dornic,[b] M. Dörr,[ay] M. Durocher,[l,h] T. Eberl,[f] D. van Eijk,[ab] I. El Bojaddaini,[av] D. Elsaesser,[ay] A. Enzenhöfer,[f,b] G. Ferrara,[l,ak] L.A. Fusco,[o,aj] T. Gal,[f] F. Garufi,[r,am] S. Gauchery,[au] S. Geißelsöder,[f] L. Gialanella,[r,ai] E. Giorgio,[l] A. Giuliante,[an] S.R. Gozzini,[j] R. Gracia Ruiz,[at] K. Graf,[f] D. Grasso,[s] T. Grégoire,[au] G. Grella,[ap] S. Hallmann,[f] H. van Haren,[ac] T. Heid,[f] A. Heijboer,[ab] A. Hekalo,[ay] J.J. Hernández-Rey,[j] J. Hofestädt,[f] G. Illuminati,[j] C.W. James,[f] M. Jongen,[ab] B. Jongewaard,[aw] M. de Jong,[ab] P. de Jong,[ab,aw] M. Kadler,[ay] P. Kalaczyński,[z] O. Kalekin,[f,1] U.F. Katz,[f] N.R. Khan Chowdhury,[j] G. Kieft,[ab] D. Kießling,[f] E.N. Koffeman,[ab,aw] P. Kooijman,[aw,az] A. Kouchner,[au] M. Kreter,[ay] V. Kulikovskiy,[q] R. Lahmann,[f] R. Le Breton,[au] F. Leone,[l,ak] E. Leonora,[p,1] G. Levi,[o,aj] M. Lincetto,[b] A. Lonardo,[t] F. Longhitano,[p] M. Lotze,[j] S. Loucatos,[au,d] G. Maggi,[b] J. Mańczak,[z] K. Mannheim,[ay] A. Margiotta,[o,aj] A. Marinelli,[ao,s] C. Markou,[aa] L. Martin,[ad] J.A. Martínez-Mora,[as] A. Martini,[m] F. Marzaioli,[r,ai] R. Mele,[r,am] K.W. Melis,[ab] P. Migliozzi,[r,1] E. Migneco,[l] P. Mijakowski,[z] L. S. Miranda,[ax] C.M. Mollo,[r,1] M. Morganti,[s,a] M. Moser,[f] A. Moussa,[av] R. Muller,[af] M. Musumeci,[l] L. Nauta,[ab] S. Navas,[ag] C.A. Nicolau,[t] C. Nielsen,[au] M. Organokov,[at] A. Orlando,[l] V. Panagopoulos,[aa] G. Papalashvili,[ae] R. Papaleo,[l]

[1]Corresponding author.

© 2018 The Author(s). Published by IOP Publishing Ltd on behalf of Sissa Medialab. Original content from this work may be used under the terms of the Creative Commons Attribution 3.0 licence. Any further distribution of this work must maintain attribution to the author(s) and the title of the work, journal citation and DOI.

https://doi.org/10.1088/1748-0221/13/05/P05035

2018 JINST 13 P05035

G.E. Păvălaş,[u] **G. Pellegrini,**[o] **C. Pellegrino,**[aj,k] **J. Pérez Romero,**[j] **M. Perrin-Terrin,**[b] **P. Piattelli,**[l] **K. Pikounis,**[aa] **O. Pisanti,**[r,am] **C. Poirè,**[q,al] **G. Polydefki,**[aa] **G.E. Poma,**[l,ak] **V. Popa,**[u] **M. Post,**[aw] **T. Pradier,**[at] **G. Pühlhofer,**[e] **S. Pulvirenti,**[l] **L. Quinn,**[b] **F. Raffaelli,**[s] **N. Randazzo,**[p] **S. Razzaque,**[ax] **D. Real,**[j] **L. Resvanis,**[y] **J. Reubelt,**[f] **G. Riccobene,**[l] **M. Richer,**[at] **A. Rovelli,**[l] **I. Salvadori,**[b] **D.F.E. Samtleben,**[ab,v] **A. Sánchez Losa,**[n] **M. Sanguineti,**[q] **A. Santangelo,**[e] **P. Sapienza,**[l] **B. Schermer,**[aw] **V. Sciacca,**[l] **J. Seneca,**[aw] **I. Sgura,**[n] **R. Shanidze,**[ae] **A. Sharma,**[ao] **F. Simeone,**[t] **A. Sinopoulou,**[aa] **B. Spisso,**[ap,r] **M. Spurio,**[o,aj] **D. Stavropoulos,**[aa] **J. Steijger,**[ab] **S.M. Stellacci,**[ap] **B. Strandberg,**[ab] **D. Stransky,**[f] **T. Stüven,**[f] **M. Taiuti,**[q,al] **F. Tatone,**[p] **Y. Tayalati,**[w] **E. Tenllado,**[ag] **T. Thakore,**[j] **P. Timmer,**[ab] **A. Trovato,**[l] **S. Tsagkli,**[aa] **E. Tzamariudaki,**[aa] **D. Tzanetatos,**[aa] **C. Valieri,**[o] **B. Vallage,**[au] **V. Van Elewyck,**[au] **F. Versari,**[o,aj] **S. Viola,**[l] **D. Vivolo,**[r,am] **M. Volkert,**[f] **L. de Waardt,**[aw] **J. Wilms,**[g] **E. de Wolf,**[ab,aw] **D. Zaborov,**[b] **J.D. Zornoza**[j] **and J. Zúñiga**[j]

[a] *Accademia Navale di Livorno, Viale Italia 72, Livorno, 57100 Italy*

[b] *Aix Marseille Univ, CNRS/IN2P3, CPPM, Marseille, France*

[c] *Cadi Ayyad University, Physics Department, Faculty of Science Semlalia, Av. My Abdellah, P.O.B. 2390, Marrakech, 40000 Morocco*

[d] *CEA, Irfu/SPP, Route Nationale, Gif-sur-Yvette, 91191 France*

[e] *Eberhard Karls Universität Tübingen, Institut für Astronomie und Astrophysik, Sand 1, Tübingen, 72076 Germany*

[f] *Friedrich-Alexander-Universität Erlangen-Nürnberg, Erlangen Centre for Astroparticle Physics, Erwin-Rommel-Straße 1, 91058 Erlangen, Germany*

[g] *Friedrich-Alexander-Universität Erlangen-Nürnberg, Remeis Sternwarte, Sternwartstraße 7, 96049 Bamberg, Germany*

[h] *Gran Sasso Science Institute, GSSI, Viale Francesco Crispi 7, L'Aquila, 67100 Italy*

[i] *KVI-CART University of Groningen, Groningen, the Netherlands*

[j] *IFIC - Instituto de Física Corpuscular (CSIC - Universitat de València), c/Catedrático José Beltrán, 2, 46980 Paterna, Valencia, Spain*

[k] *INFN, CNAF, v.le C. Berti-Pichat, 6/2, Bologna, 40127 Italy*

[l] *INFN, Laboratori Nazionali del Sud, Via S. Sofia 62, Catania, 95123 Italy*

[m] *INFN, LNF, Via Enrico Fermi, 40, Frascati, 00044 Italy*

[n] *INFN, Sezione di Bari, Via Amendola 173, Bari, 70126 Italy*

[o] *INFN, Sezione di Bologna, v.le C. Berti-Pichat, 6/2, Bologna, 40127 Italy*

[p] *INFN, Sezione di Catania, Via Santa Sofia 64, Catania, 95123 Italy*

[q] *INFN, Sezione di Genova, Via Dodecaneso 33, Genova, 16146 Italy*

[r] *INFN, Sezione di Napoli, Complesso Universitario di Monte S. Angelo, Via Cintia ed. G, Napoli, 80126 Italy*

[s] *INFN, Sezione di Pisa, Largo Bruno Pontecorvo 3, Pisa, 56127 Italy*

[t] *INFN, Sezione di Roma, Piazzale Aldo Moro 2, Roma, 00185 Italy*

[u] *ISS, Atomistilor 409, Măgurele, RO-077125 Romania*

[v] *Leiden University, Leiden Institute of Physics, PO Box 9504, Leiden, 2300 RA Netherlands*

[w] *University Mohammed V in Rabat, Faculty of Sciences, 4 av. Ibn Battouta, B.P. 1014, R.P. 10000 Rabat, Morocco*

[x] *Moscow State University, Faculty of Physics, Leninskie Gory 1, Moscow, 119991 Russia*

[y] *Physics Department, N. and K. University of Athens, Athens, Greece*

2018 JINST 13 P05035

[z] National Centre for Nuclear Research, 00-681 Warsaw, Poland
[aa] NCSR Demokritos, Institute of Nuclear and Particle Physics, Ag. Paraskevi Attikis, Athens, 15310 Greece
[ab] Nikhef, National Institute for Subatomic Physics, PO Box 41882, Amsterdam, 1009 DB Netherlands
[ac] NIOZ (Royal Netherlands Institute for Sea Research) and Utrecht University, PO Box 59, Den Burg, Texel, 1790 AB, the Netherlands
[ad] Subatech, IMT Atlantique, IN2P3-CNRS, 4 rue Alfred Kastler - La Chantrerie, Nantes, BP 20722 44307 France
[ae] Tbilisi State University, Department of Physics, 3, Chavchavadze Ave., Tbilisi, 0179 Georgia
[af] TNO, Technical Sciences, PO Box 155, Delft, 2600 AD Netherlands
[ag] University of Granada, Dpto. de Física Teórica y del Cosmos & C.A.F.P.E., 18071 Granada, Spain
[ah] University of Granada, Dept. of Computer Architecture and Technology/CITIC, 18071 Granada, Spain
[ai] Università degli Studi della Campania "Luigi Vanvitelli", Dipartimento di Matematica e Fisica, viale Lincoln 5, Caserta, 81100 Italy
[aj] Università di Bologna, Dipartimento di Fisica e Astronomia, v.le C. Berti-Pichat, 6/2, Bologna, 40127 Italy
[ak] Università di Catania, Dipartimento di Fisica e Astronomia, Via Santa Sofia 64, Catania, 95123 Italy
[al] Università di Genova, Via Dodecaneso 33, Genova, 16146 Italy
[am] Università di Napoli "Federico II", Dip. Scienze Fisiche "E. Pancini", Complesso Universitario di Monte S. Angelo, Via Cintia ed. G, Napoli, 80126 Italy
[an] Università di Pisa, DIMNP, Via Diotisalvi 2, Pisa, 56122 Italy
[ao] Università di Pisa, Dipartimento di Fisica, Largo Bruno Pontecorvo 3, Pisa, 56127 Italy
[ap] Università di Salerno e INFN Gruppo Collegato di Salerno, Dipartimento di Fisica, Via Giovanni Paolo II 132, Fisciano, 84084 Italy
[aq] Università La Sapienza, Dipartimento di Fisica, Piazzale Aldo Moro 2, Roma, 00185 Italy
[ar] Universitat Politècnica de Catalunya, Laboratori d'Aplicacions Bioacústiques, Centre Tecnològic de Vilanova i la Geltrú, Avda. Rambla Exposició, s/n, Vilanova i la Geltrú, 08800 Spain
[as] Universitat Politècnica de València, Instituto de Investigación para la Gestión Integrada de las Zonas Costeras, C/ Paranimf, 1, Gandia, 46730 Spain
[at] Université de Strasbourg, IPHC, 23 rue du Loess, Strasbourg, 67037 France
[au] APC, Université Paris Diderot, CNRS/IN2P3, CEA/IRFU, Observatoire de Paris, Sorbonne Paris Cité, 75205 Paris, France
[av] University Mohammed I, Faculty of Sciences, BV Mohammed VI, B.P. 717, R.P. 60000 Oujda, Morocco
[aw] University of Amsterdam, Institute of Physics/IHEF, PO Box 94216, Amsterdam, 1090 GE Netherlands
[ax] University of Johannesburg, Department Physics, PO Box 524, Auckland Park, 2006 South Africa
[ay] University Würzburg, Emil-Fischer-Straße 31, Würzburg, 97074 Germany
[az] Utrecht University, Department of Physics and Astronomy, PO Box 80000, Utrecht, 3508 TA Netherlands
E-mail: oleg.kalekin@physik.uni-erlangen.de, emanuele.leonora@ct.infn.it, pasquale.migliozzi@na.infn.it, maximil@na.infn.it

Abstract: The Hamamatsu R12199-02 3-inch photomultiplier tube is the photodetector chosen for the first phase of the KM3NeT neutrino telescope. About 7000 photomultipliers have been characterised for dark count rate, timing spread and spurious pulses. The quantum efficiency, the gain and the peak-to-valley ratio have also been measured for a sub-sample in order to determine parameter values needed as input to numerical simulations of the detector.

Keywords: Cherenkov detectors; Large detector systems for particle and astroparticle physics; Neutrino detectors; Photon detectors for UV, visible and IR photons (vacuum)

2018 JINST 13 P05035

Contents

1 Introduction 1

2 Quantum efficiency measurements 2

3 Gain and high voltage calibration 4

4 Timing properties and noise pulses 7

4.1 Dark count rates 8

4.2 Measurement of PMT time characteristics and of spurious pulses 9

5 Conclusions 12

2018 JINST 13 P05035

1 Introduction

KM3NeT is a large research infrastructure that will consist of a network of deep-sea neutrino detectors in the Mediterranean Sea [1–3]. The main scientific goals are neutrino astroparticle physics — the study of astrophysical objects by detecting their high-energy neutrino emission — and the investigation of neutrino properties by measuring atmospheric neutrinos. The ARCA (Astroparticle Research with Cosmics in the Abyss) detector of KM3NeT, optimised for high-energy neutrino studies, will be located off-shore Capo Passero (Italy) at 3500 m below sea level. The ORCA (Oscillation Research with Cosmics in the Abyss) detector, dedicated to low energy neutrino studies, will be located off-shore Toulon (France) at 2500 m below sea level. The KM3NeT location in the deep sea also offers interdisciplinary opportunities for continuous, real-time measurements, e.g. for marine biology, oceanography or environmental sciences.

Both detectors comprise arrays of thousands of Digital Optical Modules (DOMs). The DOMs are arranged along flexible strings, called Detection Units (DUs), kept vertical by a submerged buoy. During the first stage of the KM3NeT construction 24 DUs for the ARCA and 6 DUs for the ORCA detectors will be installed. The DOMs will detect the Cherenkov light induced in the sea water by charged particles originated in neutrino interactions. Each DOM comprises 31 3-inch PMTs hosted inside a 17-inch glass sphere.

The characteristics of the PMTs affect the detector event reconstruction accuracy. The requirements for the KM3NeT PMTs are summarised in table 1. The Hamamatsu R12199-02 PMT is the photodetector chosen for the first phase of the KM3NeT detector. It is a 80-mm diameter hemispherical PMT with 10 dynode stages and standard bi-alkali photocathode.

Given the key role played by the PMT performance in the neutrino event detection and reconstruction, the KM3NeT Collaboration has decided to perform dedicated studies on critical parameters for PMT performance and operation, including a measurement of Quantum Efficiency (QE) and calibration of time over threshold, and to fully characterise a large sample of devices as to

Table 1. Requirements for main characteristics of PMTs to be used in the KM3NeT detectors (spe is for single photoelectrons; cps is for counts per second).

Photocathode diameter	>72 mm
Nominal Voltage for gain 3×10^6	900÷1300 V
Quantum Efficiency at 470 nm	> 18%
Quantum Efficiency at 404 nm	> 25%
Peak-to-Valley ratio	> 2.0
Transit Time Spread (FWHM)	< 5 ns
Dark count rate (0.3 spe threshold, at 20 °C)	2000 cps max
Prepulses between −60 ns and −10 ns	1.5% max
Delayed pulses between 15 ns and 60 ns	5.5% max
Late afterpulses between 100 ns and 10 μs	15% max

timing and noise pulses. The results of the measurements presented in this paper will be used has input to the numerical simulations of the detector response.

The paper is organised as follows: in section 2 the setup and the method used for the measurement of the QE are presented; in section 3 the gain and Time over Threshold (ToT) dependence on the high voltage are discussed; finally in section 4 the results from the test of about 7000 PMTs are summarised.

2 Quantum efficiency measurements

The photocathode quantum efficiency is measured in DC-mode, without any amplification and with 100% collection efficiency. A voltage of −280 V is applied to the photocathode. A dedicated base is used to connect the dynodes to the input of a picoammeter. The PMT is illuminated with a xenon lamp whose light, after passing through a monochromator, produces a 1 cm spot on the photocathode. The light intensity is determined using a reference photodiode, calibrated by Hamamatsu in the wavelength range of 200÷800 nm, in steps of 10 nm with a precision of 0.1%. Reference measurements are repeated hourly. The scheme of the test setup for QE measurements is shown in figure 1. The quantum efficiency is calculated as the ratio between PMT and photodiode photocurrents weighted with the known QE of the photodiode. QE is measured in the wavelength range of interest, 280÷700 nm, in steps of 5 nm. More details on the method and on the possible systematics associated with the measurement can be found in ref. [4].

The photocathode QE has been measured for 56 PMTs chosen randomly from different production batches, in order to cross-check the measurements performed by the manufacturer on the full production. The results are presented in figure 2. Green lines represent QE curves for individual PMTs. The continuous black curve is the mean value with one standard deviation at each measured wavelength. For the wavelengths indicated in the KM3NeT specifications, the mean QE values with one standard deviation are: (26.9 ± 1.2)% (@404 nm) and (21.6 ± 1.5)% (@470 nm). The results are in agreement with the requirements.

2018 JINST 13 P05035

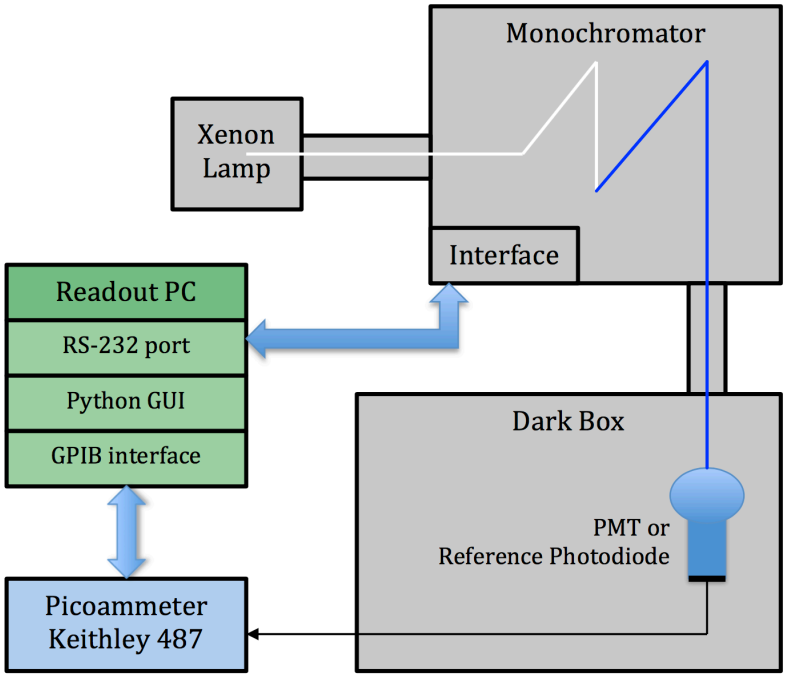

Figure 1. Scheme of the test setup for photocathode quantum efficiency measurements.

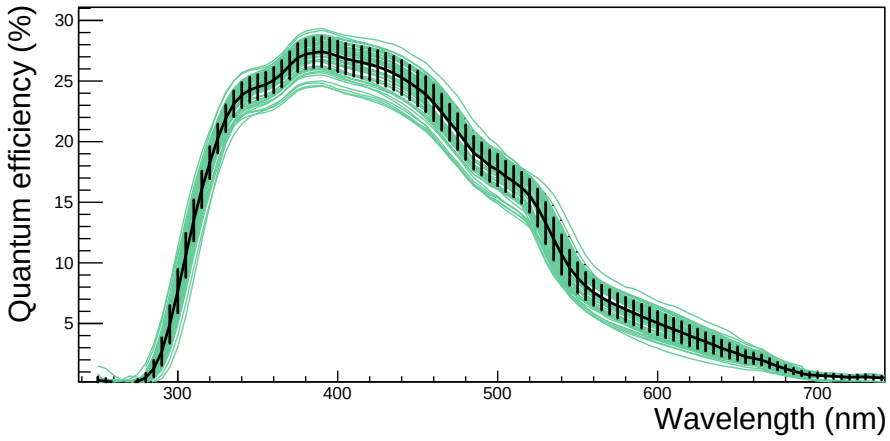

Figure 2. Photocathode quantum efficiency measurements as a function of the wavelength for 56 PMTs. The green lines show the results for individual PMTs. The continuous black curve is the mean value with one standard deviation at each measured wavelength.

2018 JINST 13 P05035

3 Gain and high voltage calibration

The manufacturer provides for each PMT the nominal high voltage (HV) needed to achieve the gain, defined as the ratio between anode and photocathode currents, of 3×10^6. However, in KM3NeT application, PMTs are not used in current, but in pulse mode. The majority of the detected pulses are due to single photoelectrons (spe). A charge distribution of spe pulses is shown in figure 3. The first peak is the so-called pedestal, the baseline signal from the PMT in absence of photon induced pulses; the red line is a Gaussian fit to the spe distribution. The gain is calculated as follows

$$G = (< SPE > - < PED >) \times (v_{\text{gain}}/50) \times \tau_{\text{step}}/(A_{\text{gain}} \times e)$$

where $< SPE >$ is the mean value of spe distribution; $< PED >$ is the mean value of the pedestal; v_{gain} is the ADC scale expressed as Volt per ADC channel; 50 (expressed in Ohm) is the ADC load resistor, i.e. the oscilloscope input impedance; τ_{step} is the sampling time step in seconds; A_{gain} is the amplification of the PMT signal performed with an amplifier; $e = 1.6022 \times 10^{-19}$ C. The following set of values has been used to obtain the plot shown in figure 3: $v_{\text{gain}} = 2.21 \times 10^{-3}$ V per ADC channel; $\tau_{\text{step}} = 10^{-9}$ s; $A_{\text{gain}} = 10$. For $(< SPE > - < PED >) \simeq 125$ ADC channels the corresponding gain is then $\sim 3.45 \times 10^6$.

Given the different methods to measure the gain, in current mode by Hamamatsu and in pulse mode by KM3NeT, differences in nominal voltages are expected. Therefore, a method of HV tuning in order to get the 3×10^6 gain in pulse mode has been developed.

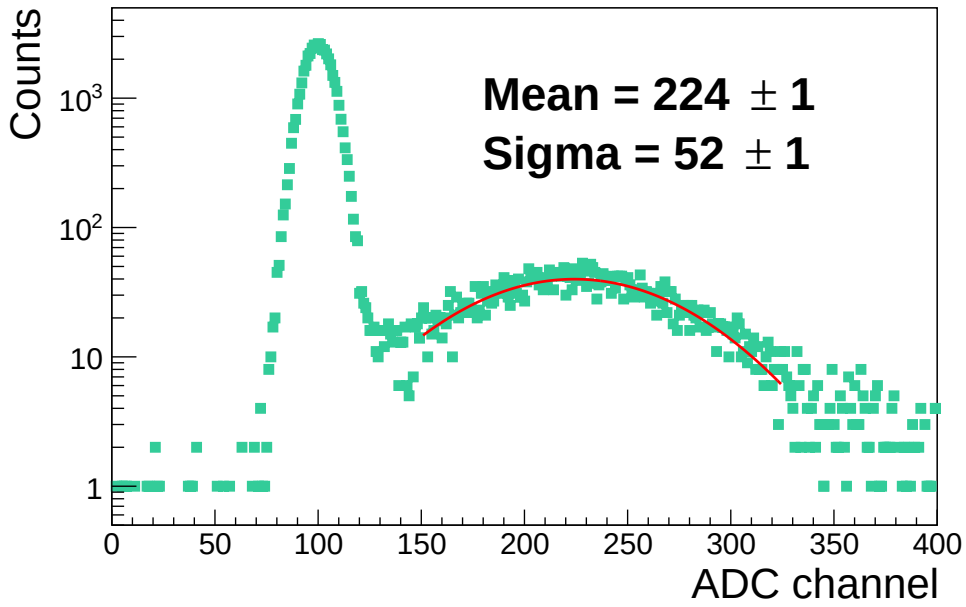

Figure 3. Single photoelectron charge distribution for a typical PMT. The red line shows the Gaussian fit to the spe distribution.

The nominal HV has been determined for a sub-set of 66 PMTs with resistive bases having a high voltage division ratio of 3 between the photocathode and the first dynode, and of 1 between all

2018 JINST 13 P05035

other dynodes, as specified by the manufacturer. In a dark box the whole PMT surface is uniformly illuminated by fast LED pulses (460 nm central value with a 800 ns FWHM) at 1 kHz frequency. Light from the pulser is delivered to the dark box via an optical fiber. A diffusor is installed at the fiber output at a distance of ∼1 m from the PMT. The pulser amplitude is tuned to obtain a mean number of ∼0.1 photons per pulse detected by the PMT. The signal is amplified ten times and sent to a LeCroy Waverunner 6100 oscilloscope. The latter is triggered with the sync signal from the pulser and the waveforms of PMT signals are saved with a sampling rate of 10^9 samples per second. The gain is calculated integrating the signal within a gate of 20 ns and fitting the distribution with a Gaussian function. Measurements of the gain are performed at seven different voltages in steps of 25 V around the HV value provided by the manufacturer. These results are used to fit the gain-HV linear dependence in a double logarithmic scale (gain slope). The HV value corresponding to a gain of 3×10^6 is calculated from the fit with 1 V precision.

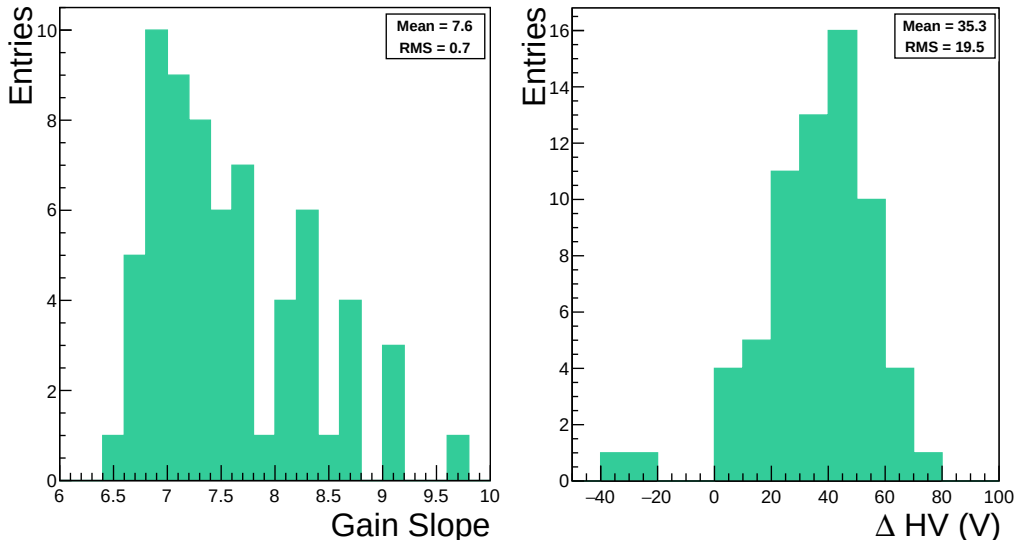

Figure 4. Left: distribution of the HV gain slope (see text for the definition). Right: difference between the determined high voltage values and those provided by the manufacturer to achieve a 3×10^6 gain.

In figure 4-left the histogram with the gain slopes is shown. The HV values to achieve the 3×10^6 gain derived from these measurements have been compared to those provided by the manufacturer. The difference between these two values is presented in figure 4-right. The systematic difference can be explained with the different methods used for gain measurement. The peak-to-valley ratio has been measured for same sample of 66 PMTs using the new set of HV values determined in pulse mode. The definition of the peak-to-valley ratio is shown in figure 5-left. This parameter is connected to the capability of a PMT to discriminate single photoelectron signals, larger values corresponding to a better discrimination. The measured distribution of the peak-to-valley ratio is shown in figure 5-right.

A dedicated base has been developed for operating the PMTs inside the KM3NeT DOMs [5]. These bases are equipped with current amplifiers, whose output is proportional to the charge of the initial pulse. Amplified signals have a long trailing tail with lengths proportional to the amplitude.

2018 JINST 13 P05035

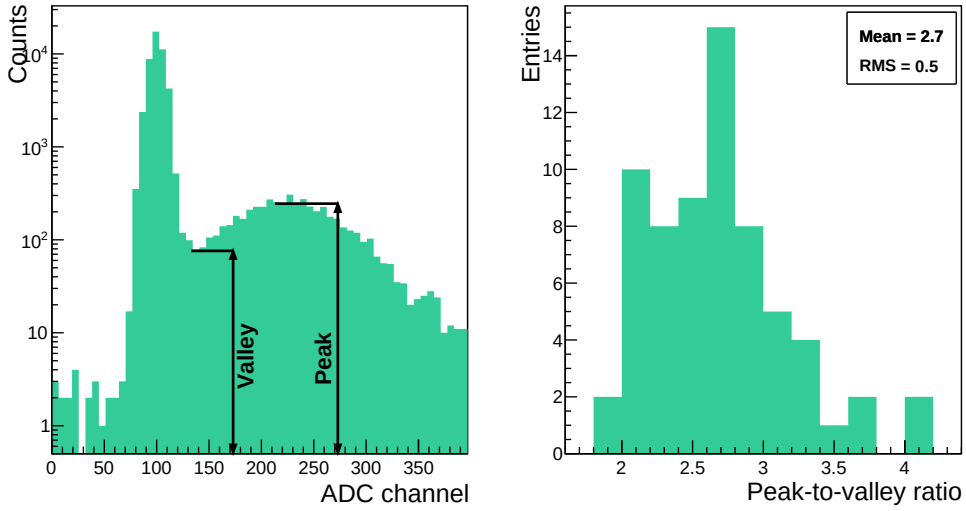

Figure 5. Peak-to-Valley ratio. Left: definition of the parameter; right: distribution of the measurements for the sub-sample of 66 PMTs.

Spe pulses after the amplification have an amplitude of ~500 mV. A tunable threshold discriminator on the base provides a rectangular ToT signal which is sent to the Central Logic Board (CLB) of the DOM for digitisation. In normal operation, only ToT signals are digitised and the base dissipates only 3.3 mW. The base allows also to read out the amplified analogue signal. In this case the power consumption increases, but this feature allows for threshold and ToT calibration in the laboratory where the power consumption is not critical. Both analogue and ToT are generated as differential signals. An example is shown in figure 6.

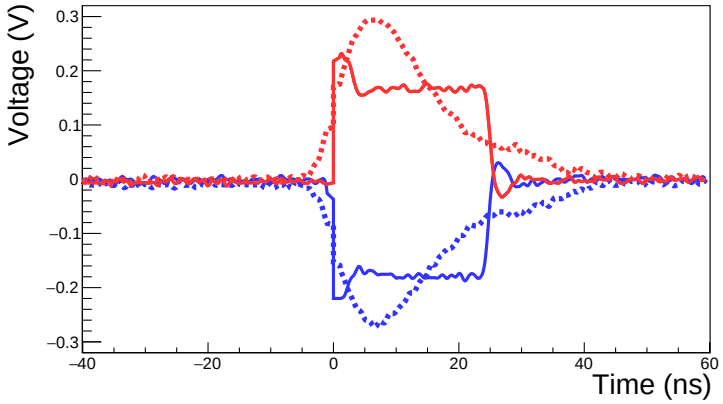

Figure 6. Analogue (dashed lines) and ToT (solid lines) signals from the KM3NeT PMT base. Colors indicate positive and negative parts of the differential signals, red-positive, blue-negative.

A correct interpretation of the ToT is needed for a correct usage of the data collected by the PMTs in the apparatus. A threshold-ToT calibration has been therefore performed on a sub-set of 5 of the 66 calibrated PMTs, equipped with the KM3NeT active bases. The procedure works as follows. The derived HV for the 3×10^6 gain is applied and a few spe data sets are taken

2018 JINST 13 P05035

with different thresholds set on the bases. Using the amplitude distribution of the analogue signal, thresholds are derived and then expressed as a fraction of spe. The value of 0.3 spe is chosen as a default threshold. This level of the threshold allows detection a large fraction of spe signal and at the same time is well separated from the noise. The final measurement at nominal HV and default threshold has been performed. The derived ToT distribution is peaked at 26.4 ns, see figure 7. This value has been chosen as a nominal ToT for spe.

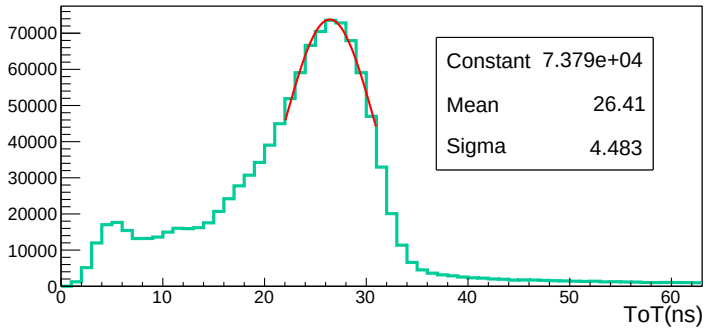

Figure 7. Typical ToT distribution. The curve shows the fit of peak whose value corresponds to 26.4 ns.

4 Timing properties and noise pulses

A special device (DarkBox) has been developed [6] to calibrate a large sample of PMTs and validate the manufacturer production. The PMTs are tested as prepared for integration in the DOMs, i.e. they are equipped with their bases and coated with the same insulating varnish used for the bases [7]. The DarkBox is shown schematically in figure 8. It consists of a wooden box equipped with removable trays designed to hold the PMTs under test. A time calibrated electrical cabling system has been made to connect PMTs to the data acquisition system placed outside the box, maintaining the same time signal delay for all PMTs. The data acquisition system is built replicating the electronics system of the DOMs, which includes for each set of 31 PMTs a control board equipped with two signal collection boards (the 'octopuses' in figure 8) interfacing the PMTs. Subnanosecond synchronisation of the control boards is achieved by means of White Rabbit [6]. A picosecond accuracy laser and a calibrated optical splitting system are used to illuminate all PMTs at spe level. Details on the mechanics, the electronics and the laser calibration system as well as on its performance can be found in [6].

Hereafter the results obtained by testing 6960 PMTs are presented.

The accurate, but time consuming, HV tuning procedure described in section 3 is not possible for the PMTs installed in the apparatus and is not viable when testing a large number of PMTs. For this case, the PMT gains are equalised based on the indirect observable of the ToT value. For each PMT the HV value is set in order to have the peak value of the time over threshold distribution at 26.4 ns, for a spe signal at 0.3 spe threshold. These values are referred to as the "tuned HV".

During a run with laser, the ToT distribution of the first hit is collected. This distribution has a peak in the range 26–27 ns confirming the reliability of the automatic HV calibration tuning.

The results discussed in the following sections have been obtained with tuned HV.

2018 JINST 13 P05035

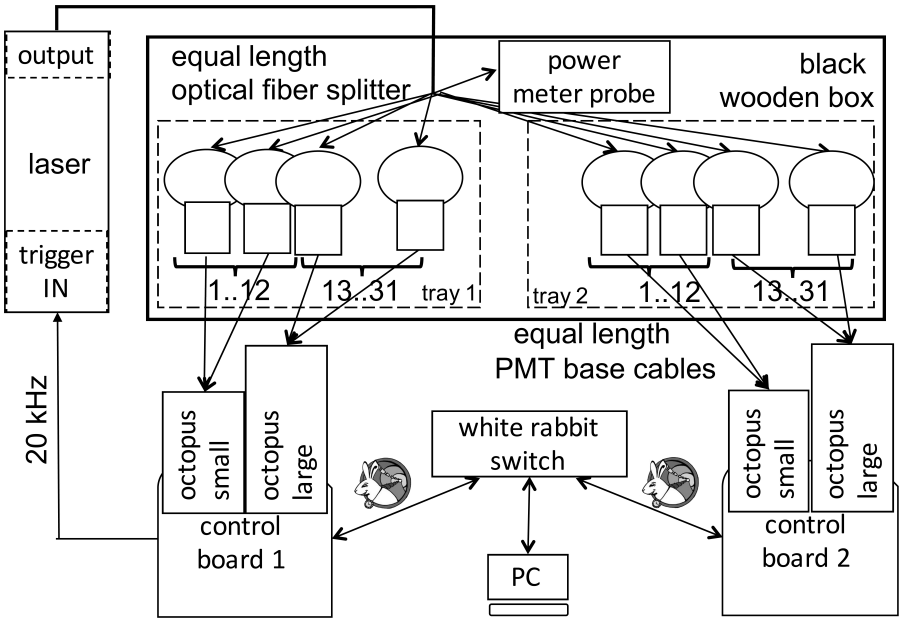

Figure 8. DarkBox experimental setup scheme. The details can be found in ref. [6].

4.1 Dark count rates

The dark counts are random noise pulses that can be measured at the anode of a PMT even in total darkness. The most significant source of random noise for a PMT is the spontaneous thermionic emission of electrons by the photocathode. Pulses that result from this process correspond mainly to a spe. The rate at which these pulses are observed is proportional to the photocathode area and varies considerably depending on the photocathode material. Bialkali photocathodes (as those used in KM3NeT PMTs) have the lowest ratio per unit area. Another source of dark pulses is the natural radioactivity in the structure of the PMT itself. The most important components are usually ^{40}K and Th contained in the glass envelope. β particles emitted in radioactive decays will give rise to a flash of Cherenkov radiation that can produce photoelectron emission from the photocathode [8].

Once the PMTs are fed with the tuned HV, dark count rates are monitored for 9 hours. During this time, the PMT recover from the initial exposure to the light and the dark count rate becomes stable. The measured rate is the average over the last 100 s of the run for each PMT. The results are shown in figure 9. The average dark count rate is about 1300 cps, while the fraction of PMTs above 2000 cps is 7.1%. These PMTs were tested again after a longer darkening (48 hours) reducing the fraction of PMTs not to be integrated in the KM3NeT DOMs to 3.5%. The average dark count rate of good PMTs is about 700 cps.

The effect of the artificial light on the dark count rate has been also studied. Two different artificial light sources have been used: fluorescent tube lamps and LED lamps. The dark count rate for six PMTs was initially measured in the DarkBox after several weeks of darkening. For all of them the measured dark count rate was below 200 cps. These PMTs were then exposed for two hours to a fluorescent tube lamp light before the dark count rate measurement started. It took about a week of darkening to stabilise the dark count rate at the value previously measured. The

2018 JINST 13 P05035

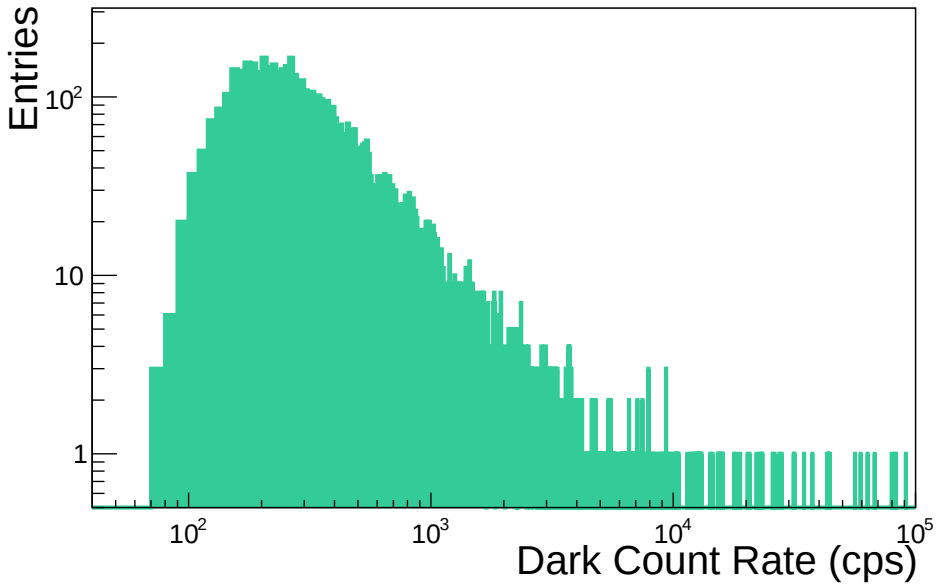

Figure 9. Dark Count rate for the full PMT sample characterised.

same measurement was then performed after a two hour exposure to a LED lamp light.[1] It took 4 hours to stabilise the dark count rate at the value previously measured initially. Therefore, it can be concluded that laboratories where PMTs are handled should ideally be equipped with LED lamps.

4.2 Measurement of PMT time characteristics and of spurious pulses

Unlike dark counts, spurious pulses are time-correlated with the expected PMT response to light. Indeed, they can come early or can be delayed by a characteristic time with respect to the electron transit time through the PMT. They are usually classified as prepulses, delayed pulses and afterpulses. The tests illustrated in this section have been made by collecting 10-minutes runs while illuminating the PMTs with a 470 nm laser, after the needed darkening time. The laser trigger frequency was set to 20 kHz and its light output tuned so as to operate the PMTs in the spe regime (0.1 photoelectron per pulse). These data have been analysed to estimate PMT timing performances and measure the fraction of spurious pulses.

Timing distribution. Time characteristics of PMTs have been measured by detecting and analysing the so-called first photon hits, i.e. pulses detected in a window of 200 ns around the expected arrival time of the PMT signal. The distribution of arrival time of the first hits for a typical PMT is shown in figure 10a. The main peak of the distribution corresponds to the PMT transit time (TT) and the transit time spread (TTS) is defined as the FWHM of this peak. The distribution of the TTS is shown in figure 11. All values are below 5 ns.

Determination of prepulses and delayed pulses. To evaluate the average probability of occurrence of spurious pulses the arrival time distributions of all PMTs have been shifted by subtracting the transit time, normalised and then summed up. The resulting distribution, normalised as to

[1] LED lamps with color in the range 3000–6000 K lead to similar results.

2018 JINST 13 P05035

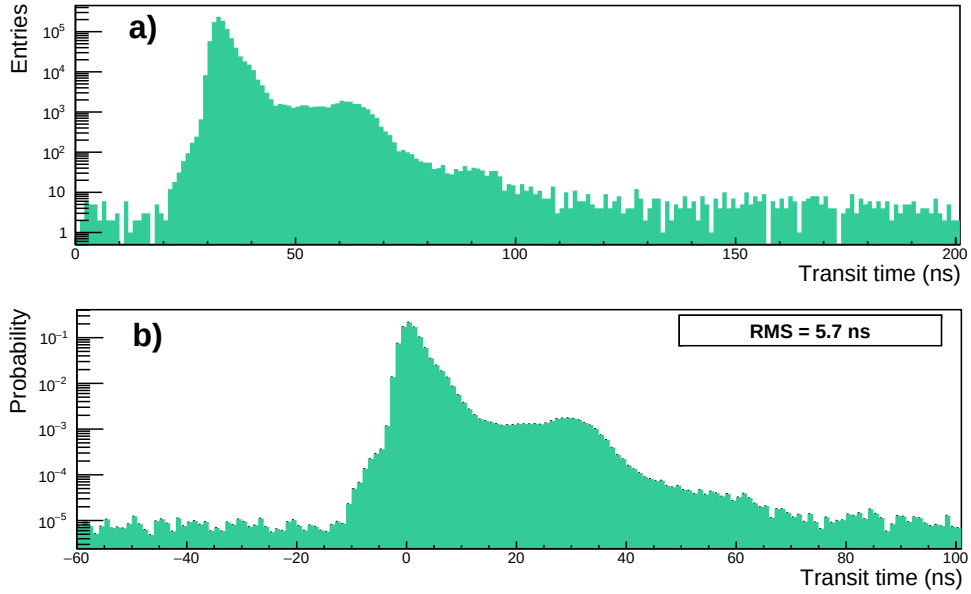

Figure 10. Distribution in a) of arrival time of the first hits for a typical PMT and in b) of arrival time of the first hits normalised as to obtain the average probability for spurious pulses.

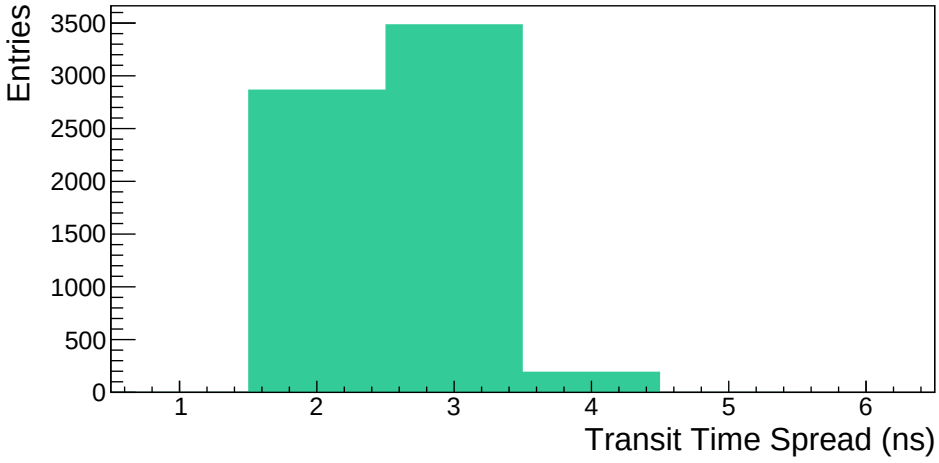

Figure 11. Transit Time Spread for the full PMT sample characterised.

obtain the average probability for spurious pulses, is shown in figure 10b. Prepulses, that arise from a direct photoeffect on the first dynode due to photons that pass through the photocathode without interacting [9], appear as a non Gaussian tail on the left side of the main peak.

For a 3-inch PMT the prepulse arrival time is in the range $10 \div 60$ ns before the main pulse. However, a more conservative approach has been adopted and a range $10 \div 60$ ns before the main pulse has been considered. The percentage of prepulses is defined as the ratio of the hits in the window $[T_{\text{peak}} - 60.5\,\text{ns}, T_{\text{peak}} - 10.5\,\text{ns}]$ over the number of the first hits; T_{peak} corresponds to the centre of the maximum bin (transit time peak).

2018 JINST 13 P05035

The distribution of the prepulses measured for the tested PMTs is shown in figure 12. 98.8% of the total sample has a prepulse fraction below 1.5%. The average prepulse fraction is 0.2%.

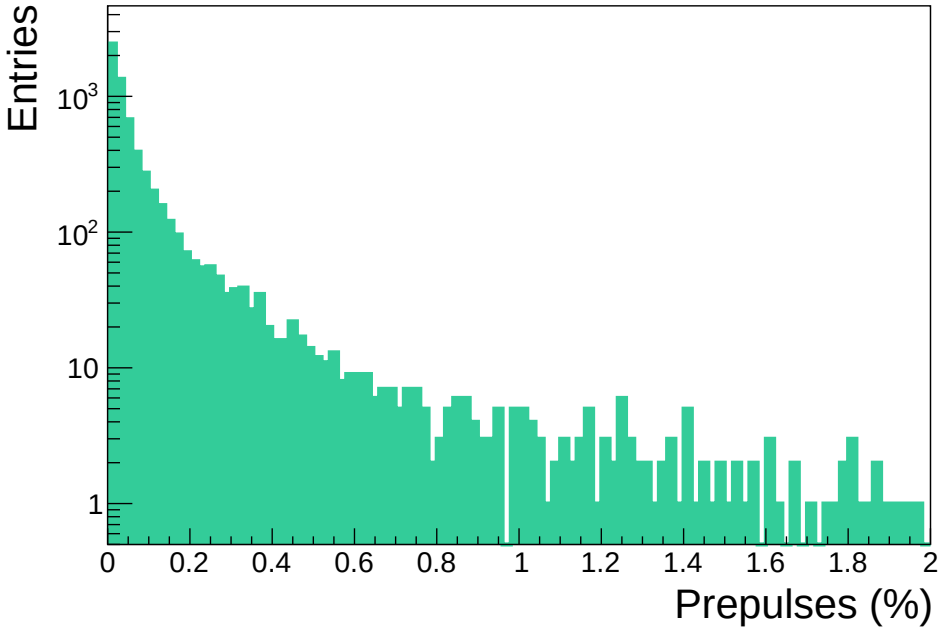

Figure 12. Distribution of the prepulse fraction for the full PMT sample characterised.

Delayed pulses are due to elastic scattering of photoelectrons on the first dynode [9]. A photoelectron hitting the first dynode may be backscattered without liberating any secondary electron. Backscattered photoelectrons on the first dynode are decelerated by the electric field and then accelerated again towards it, extracting secondary electrons. Thus, also delayed pulses are detected as the response of the PMT to a light event. Delayed pulses do not have a random time distribution, but they tend to accumulate around a time that is twice the photocathode to the first dynode transit time. Therefore, delayed pulses distort the falling edge of the main peak and give rise to a bump at $\sim$ 35 ns as shown in figure 10b. The percentage of delayed pulses has been calculated as the ratio of the first hits in the window $[T_{\text{peak}} + 15.5\,\text{ns}, T_{\text{peak}} + 60.5\,\text{ns}]$ over the number of all first hits.

The distribution of the delayed pulses measured for the tested PMTs is shown in figure 13. 98.5% of the total sample has a delayed fraction below 5.5%. The average delayed pulse fraction is 3.2%.

Determination of afterpulses. Afterpulses are noise pulses that follow the main PMT response to a detected light event. They can be classified as early (Type I) or late (Type II) afterpulses. Type I afterpulses are due to the emission of light from the stages of the multiplier structure, which can reach the photocatode producing further photoelectrons. In general PMTs exhibit Type I afterpulses in the time window $10 \div 80$ ns after the primary pulse. Type II afterpulses are caused by residual gases that can be ionised by the passage of electrons in the space between the photocathode and the first dynode and also through the multiplier structure. The positive ions that are formed will drift backward and some can find a path back to the photocathode. Since the drift velocity of the positive ions is low, the time taken to return to the photocathode can range from hundreds of nanoseconds to

2018 JINST 13 P05035

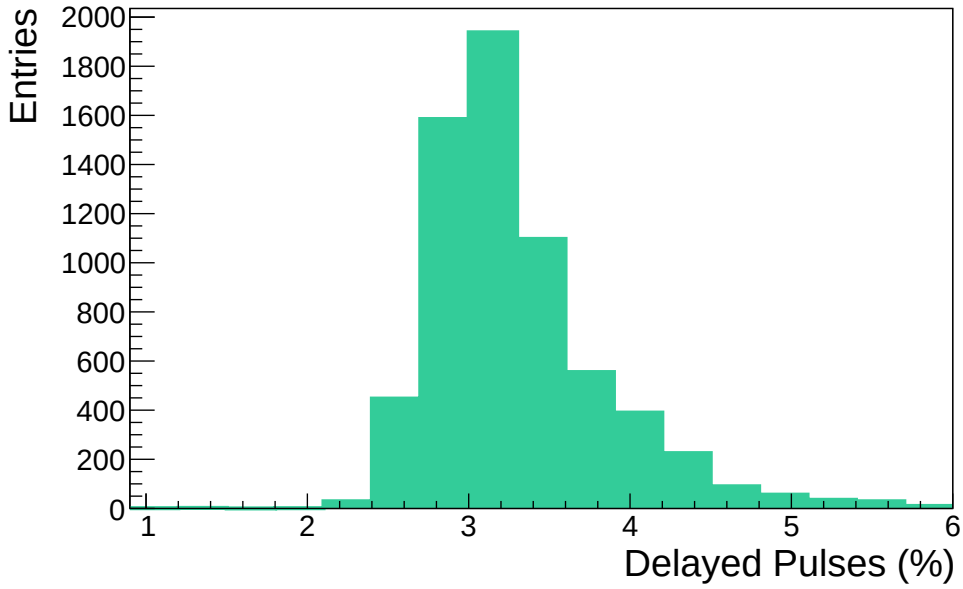

Figure 13. Distribution of the delayed pulse fraction for the full PMT sample characterised.

tens of microseconds. It also depends on the type of ions, on the position where they are generated and on the supply voltage.

In a 3-inch PMT, Type I afterpulses arrive within ~ 20 ns after the first hits.Since the KM3NeT front-end electronics does not allow for a separation of consecutive hits with a time difference $\lesssim$26 ns, no direct measurement of early afterpulses is possible with the current setup.

Afterpulses were studied by analysing the ToT versus transit time correlation (figure 14). In this plot four regions with long transit time and ToT exceeding the spe signal can be identified. These events are due to the residual gases inside the PMT. Given the typical drift velocity of each ion, the one located at transit time of $\sim 1 \div 1.5\,\mu$s is presumably produced by CH_4 ions, the one at $\sim 3 \div 4\,\mu$s by Cs ions. Other regions located below 1 μs transit time are due to hydrogen and helium ions. The percentage of Type II afterpulses is determined as the ratio of afterpulses in the time window $[T_{\text{peak}} + 100.5\,\text{ns}, T_{\text{peak}} + 10\,\mu\text{s}]$ over the total number of hits.

The percentages of spurious pulses of all types are corrected taking into account the dark noise hits that contaminate both first hits and spurious pulse distributions.

The histogram of the afterpulse fraction measured for the whole PMT sample is shown in figure 15. 92.4% of the total sample has an afterpulse fraction below 15%. The average afterpulse fraction is 7.1%.

5 Conclusions

A large sample of PMTs, consisting of about 7000 3-inch Hamamatsu type R12199-02, has been fully characterised and calibrated in order to assess its performance with a high degree of accuracy. In order to check the quality of the supplied detectors, at first we randomly selected PMTs and measured quantities that routinely monitored by the manufacturer. Therefore, for a sub-sample of about 60 PMTs also the QE, the gain and the peak-to-valley ratio have been measured and the results

2018 JINST 13 P05035

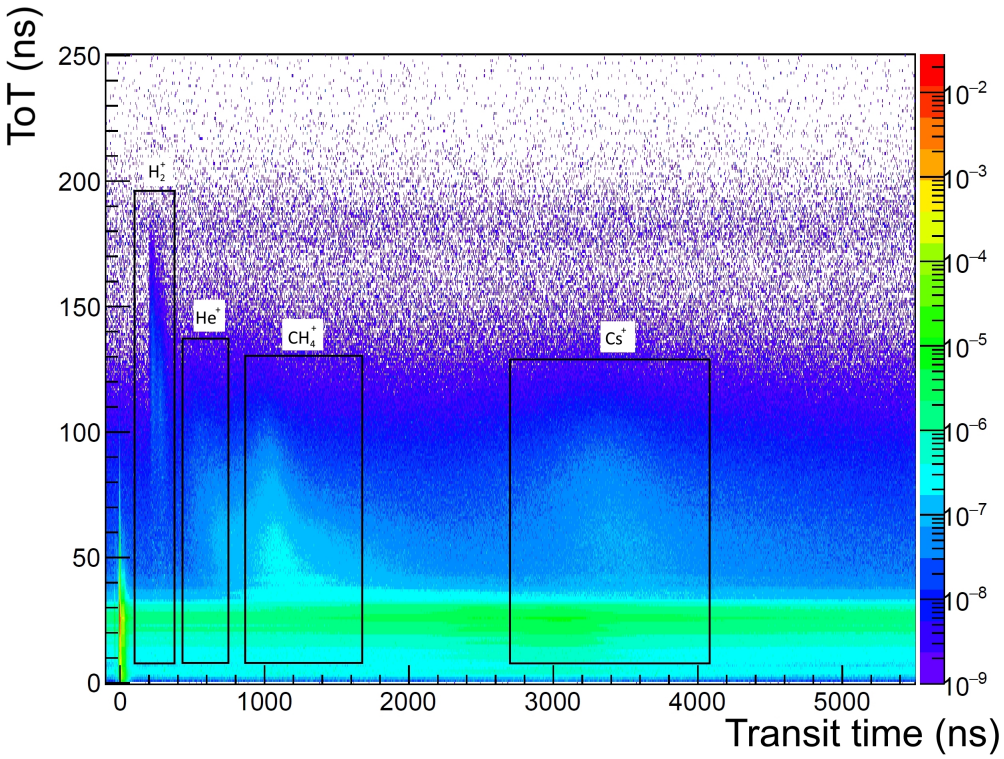

Figure 14. ToT as a function of the first hit time. The regions corresponding to signals induced by different ions are also indicated. Note that the scale on the right shows the probability for a given couple (TOT;TT) to occur. The integral over the whole plane is 1.

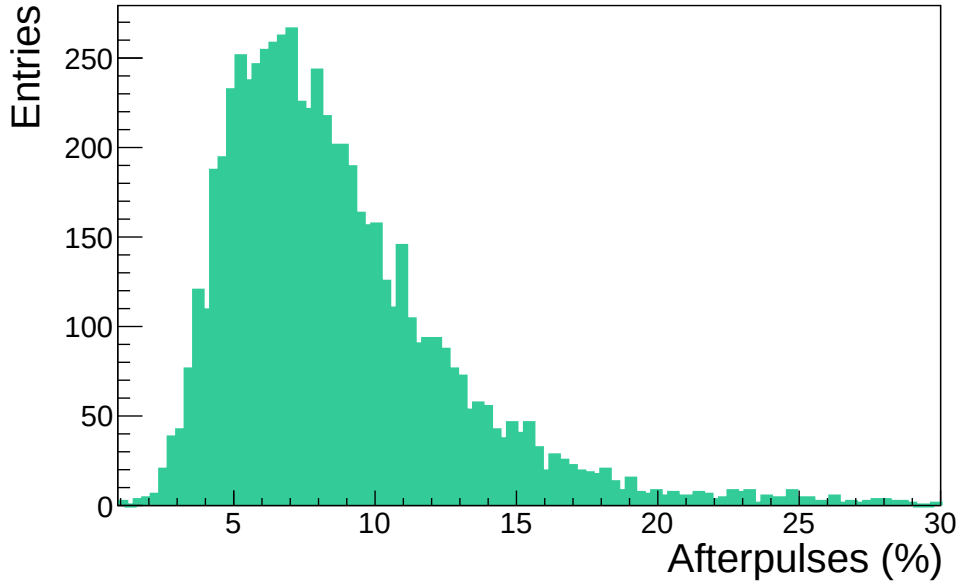

Figure 15. Afterpulse distribution for the full PMT sample characterised.

2018 JINST 13 P05035

found in agreement with the expectations. The results of these measurements will be used as input to numerical simulations of the KM3NeT detector.

For a full characterisation of the sample in terms of the main parameters such as dark counts, TTS and spurious pulse fractions, a fast and reliable procedure has been set up to measure these quantities and measurements have been performed on almost 7000 tubes. These tests allowed to identify a small fraction ($\sim$ 7%) of PMTs that do not comply with the specifications given by the KM3NeT Collaboration.

Acknowledgments

The authors acknowledge the financial support of the funding agencies: Agence Nationale de la Recherche (contract ANR-15-CE31-0020), Centre National de la Recherche Scientifique (CNRS), Commission Européenne (FEDER fund and Marie Curie Program), Institut Universitaire de France (IUF), IdEx program and UnivEarthS Labex program at Sorbonne Paris Cité (ANR-10-LABX-0023 and ANR-11-IDEX-0005-02), France; 'Helmholtz Alliance for Astroparticle Physics' funded by the Initiative and Networking Fund of the Helmholtz Association, Germany; The General Secretariat of Research and Technology (GSRT), Greece; Istituto Nazionale di Fisica Nucleare (INFN), Ministero dell'Istruzione, dell'Università e della Ricerca (MIUR), Italy; Agence de l'Oriental and CNRST, Morocco; Nederlandse organisatie voor Wetenschappelijk Onderzoek (NWO), the Netherlands; National Authority for Scientific Research (ANCS), Romania; Plan Estatal de Investigación (refs. FPA2015-65150-C3-1-P, -2-P and -3-P, (MINECO/FEDER)), Severo Ochoa Centre of Excellence and MultiDark Consolider (MINECO), and Prometeo and Grisolía programs (Generalitat Valenciana), Spain.

References

[1] KM3NeT collaboration, S. Adrián-Martínez et al., *Letter of intent for KM3NeT 2.0*, *J. Phys.* **G 43** (2016) 084001 [arXiv:1601.07459].

[2] KM3NeT collaboration, S. Adrián-Martínez et al., *Deep sea tests of a prototype of the KM3NeT digital optical module*, *Eur. Phys. J.* **C 74** (2014) 3056 [arXiv:1405.0839].

[3] KM3NeT collaboration, S. Adrián-Martínez et al., *The prototype detection unit of the KM3NeT detector*, *Eur. Phys. J.* **C 76** (2016) 54 [arXiv:1510.01561].

[4] B. Herold, O. Kalekin and J. Reubelt, *PMT characterisation for the KM3NeT project*, *Nucl. Instrum. Meth.* **A 639** (2011) 70.

[5] P. Timmer, E. Heine and H. Peek, *Very low power, high voltage base for a photo multiplier tube for the KM3NeT deep sea neutrino telescope*, 2010 *JINST* **5** C12049.

[6] C.M. Mollo et al., *A new instrument for high statistics measurement of photomultiplier characteristics*, 2016 *JINST* **11** T08002 [arXiv:1604.03922].

[7] KM3NeT collaboration, S. Adrián-Martínez, *A method to stabilise the performance of negatively fed KM3NeT photomultipliers*, 2016 *JINST* **11** P12014.

[8] G.F. Knoll, *Radiation detection and measurements*, John Wiley Sons, Inc. (1999).

[9] B.K. Lubsandorzhiev, R.V. Vasiliev, Y.E. Vyatchin and B.A.J. Shaibonov, *Photoelectron backscattering in vacuum phototubes*, *Nucl. Instrum. Meth.* **A 567** (2006) 12 [physics/0601157].

2018 JINST 13 P05035